Article

Design of Monolithic Bi-Layer High-Z PAL-Si Hard X-ray CMOS Image Sensors for Quantum Efficiency Enhancement

Eldred Lee [1,2], Kevin D. Larkin [1], Xin Yue [1], Zhehui Wang [2], Eric R. Fossum [1] and Jifeng Liu [1,*]

1   Thayer School of Engineering, Dartmouth College, Hanover, NH 03755, USA
2   Los Alamos National Laboratory, Los Alamos, NM 87545, USA
*   Correspondence: jifeng.liu@dartmouth.edu

Abstract: This article experimentally investigates the inception of an innovative hard X-ray photon energy attenuation layer (PAL) to advance high-energy X-ray detection (20–50 keV). A bi-layer design with a thin film high-Z PAL on the top and Si image sensor on the bottom has previously demon-strated quantum yield enhancement via computational methods by the principle of photon energy down conversion (PEDC), where high-energy X-ray photon energies are attenuated via inelastic scattering down to $\leq$10 keV, which is suitable for efficient photoelectric absorption by Si. Quantum yield enhancement has been experimentally confirmed via a preliminary demonstration using PAL-integrated Si-based CMOS image sensors (Si CIS). Furthermore, substituting the high-Z PAL with a lower-Z material—Sn—and alternatively coupling it with a conventional scintillator ma-terial—Lutetium-yttrium oxyorthosilicate (LYSO)—have been compared to demonstrate the most prominent efficacy of monolithic integration of high-Z PAL on Si CIS to detect hard X-rays, paving the way for next-generation high-energy X-ray detection methods.

Keywords: X-ray photonics; high-Z materials; X-ray detection; photon attenuation; image sensors

1. Introduction

Hard X-ray detection at photon energies >20 keV has broad applications in high-energy physics, materials science, and biomedical imaging. In our previous work [1], we presented and computationally demonstrated a new concept for the direct detection of high-energy X-ray photons by using a μm-scale high-Z thin film—the "photon attenuation layer" (PAL). The PAL is designed to attenuate the incident photon energy below 10 keV, thereby allowing for more efficient absorption of down-converted X-ray photons by Si detectors underneath, or more generally, an "electron generation layer" (EGL). This innovative concept, which is schematically represented in Figure 1a, possesses great potential to surpass the performance of state-of-the-art X-ray detectors based on Si CCD or photocathodes and well-established scintillation- and CdTe-based methods.

There have recently been significant efforts to increase the total efficiency of scintillation-based methods. Still, the enhancements observed so far have been unremarkable, and the total efficiency remains low due to the light extraction efficiency being limited by total internal reflection. The current state-of-the-art CdTe-based methods require considerably thick layers (mm-scale) of the material, which will limit the response time of the devices [1,2]. The simple yet highly effective device structure of the computationally simulated high-Z PAL-Si bi-layer concept in [1] and its underlying principle of X-ray photon energy down-conversion (PEDC) have the potential to transform X-ray detection with regards to spatial resolution and response time if the detection enhancement can be experimentally demonstrated.
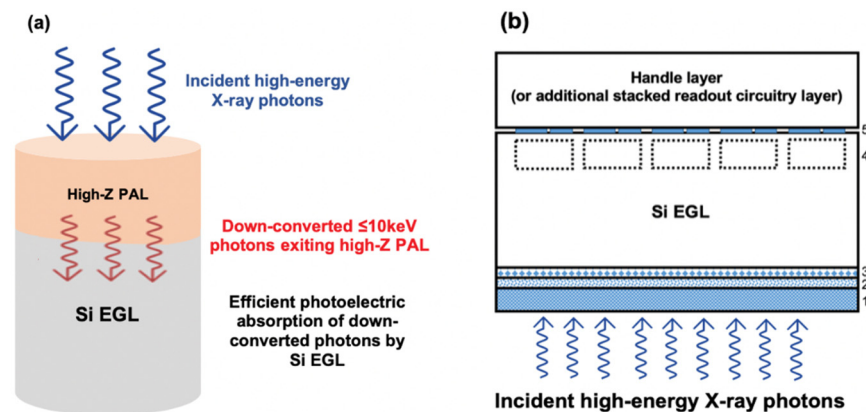
Figure 1. (**a**) Schematic showing the mechanism of the high-Z PAL-Si EGL detector design. High-energy X-ray photons (shown with blue arrows) are incident to the top of the high-Z PAL. Incident photons are down-converted (i.e., redshifted, as shown with red arrows) via inelastic scattering in the high-Z PAL and undergo efficient photoelectric absorption by Si. It must be noted that the number of red arrows is only schematic and does not mean that one high-energy photon converts into two or more low-energy photons. (**b**) Representation of the expected cross-section of a backside illuminated CIS- or quanta image sensor (QIS)-based device with PAL-EGL integration. Layers are as follows: 1 is high-Z PAL, and 2 is a thin (<100 nm) backside passivation oxide (e.g., SiO_2) that can be added between PAL and Si for practicality, but the overall QY should not be affected because down-converted X-ray photons can readily penetrate through the oxide layer. Additionally, 3 represents optional implants or epitaxial growth for surface pinning, 4 signifies pixelated carrier storage wells, and 5 denotes frontside pixel readout circuitry. Reused by the authors from [1] based on MDPI open access Creative Commons CC BY 4.0 license.

Figure 1b further illustrates the capability of monolithic integration with Si-based CIS [1], which suggests that the PAL-enhanced image sensors can pave the way toward wide field-of-view X-ray camera designs for synchrotron and X-ray free electron laser light source applications [3,4]. The modeling in the previous work can also guide experimental verification toward high-resolution, high-efficiency X-ray detection using PAL-enhanced Si CIS and future advances in the X-ray cameras for these applications.

In this work, a detailed process flow to fabricate high-Z PAL-CIS is discussed. Using the previous theoretical modeling in [1] as a guide, we present experimental results and verifications of the hard X-ray (20–50 keV) detection signal and quantum efficiency (QE) enhancements from the Si direct detection method using monolithic integration of high-Z Bi_2Te_3 PAL on Si CIS. Moreover, to further verify the high-Z PAL mechanism and superior performance, the substitution of high-Z Bi_2Te_3 with lower-Z Sn and coupling with the traditional scintillator material Lutetium Yttrium Silicate (LYSO) were also assessed and compared. Monolithic integration of a high-Z PAL on Si CIS outperforms the low-Z material and the coupling with the LYSO scintillator material. Overall, a QE enhancement of 3–10× is demonstrated for 20–50 keV X-ray photon energy, verifying our theoretical predictions in [1].

2. Post-Processing for PAL Integration on Si CMOS Image Sensors

2.1. Motivation and Challenges

As indicated in [1], the quantum yield (QY) of Si X-ray detectors with high-Z PAL as a down-conversion layer on top exceeded those of the existing state-of-the-art research work. However, it should be emphasized that all results shown in [1] are computational; thus, device fabrication and physical testing were conducted in this work to verify the computational efforts.

Frontside illuminated CMOS image sensor (CIS) chips have been designed for tapeout at a foundry using a standard 180 nm CIS process. These Si CIS chips were post-processed

at Dartmouth for PAL integration. The provided chips are small, with an area of approximately 9.12 mm² for the entire chip and a 2.48 mm² active pixel region area (50 μm pixel pitch, 31 × 32 pixel array). This poses challenges in lithography since mask aligners are optimized for full wafers. Therefore, for the purpose of PAL deposition, the chips must be carefully handled during the cleanroom process, as there are large probabilities of error leading to chip damage due to their minuscule nature. The size of the provided CIS poses various challenges during the post-processing procedures, including and not limited to non-uniformity in photoresist spin coating causing significant edge beads, incapability of undergoing photolithography using a contact mask due to non-uniform and non-planar surface caused by the photoresist edge beads and carrier wafer coupon adhesive. Furthermore, physically handling the chips from station to station could cause physical damage to the chips. PAL deposition and strip processes also pose challenges because high-Z PAL thin films are sputtered instead of evaporated on the patterned Si CIS chips. The relatively conformal deposition on the sidewalls of the photoresist can lead to issues when lifting off relatively thick PAL layers $\geq$ 500 nm. These challenges can cause a low yield rate for producing acceptable-quality chips that can eventually be wire-bonded and packaged. However, despite the challenges that were raised during the post-processing steps, mitigation solutions were found for these issues. Several chips have been successfully post-processed with acceptable quality, which led to successful wire bonding and packaging.

### 2.2. Process Flow of High-Z PAL Integration on CIS

As aforementioned, frontside illuminated CIS chips need to be post-processed so that the dielectric layers in the pixel active region can be eliminated via etching to expose Si, and high-Z PAL thin-film can be deposited directly on top of Si. Figure 2 represents the high-level process flow that has been developed to appropriately integrate high-Z PAL on CIS pixel active regions.
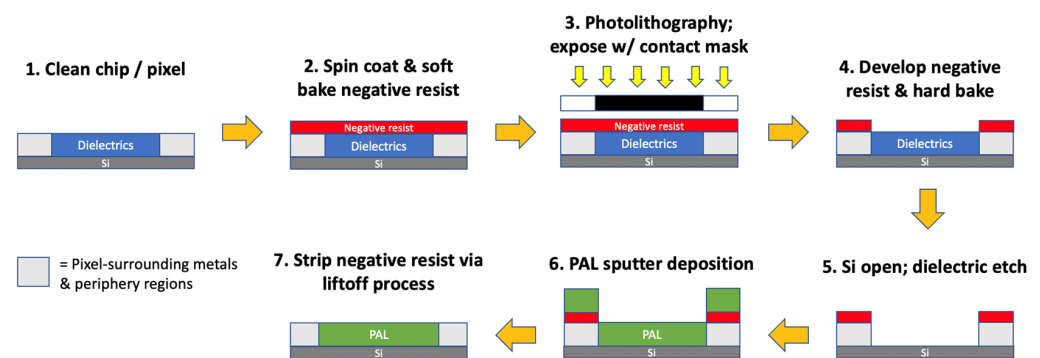
**Figure 2.** High-level process flow for PAL integration on Si CIS.

It should be noted that due to the minuscule nature of the provided CIS chips, they were bonded to a carrier coupon (i.e., a small Si coupon) via an adhesive such as Crystalbond for secure post-processing. This carrier coupon bonding process is omitted in Figure 2.

To summarize the high-level process flow represented in Figure 2, a thin layer of negative-tone liftoff resist (AZ nLOF 2035; LOR) was spin-coated at 700 RPM for 10 s and 4000 RPM for 60 s and baked on the CIS. This was followed by photolithography with a contact mask custom-designed to protect the pixel-surrounding metals and periphery regions and expose the remainder of the pixel-active region. A cartoon schematic of a single pixel of the CIS chip with surrounding metals can be seen in Figure 3, and the contact mask must be designed to protect the metals. Note that a cartoon has been provided in this article rather than an SEM image to protect the manufacturer's IP. A schematic of the custom-designed contact mask can also be seen in Appendix A.
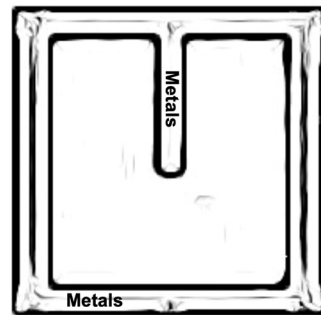
Figure 3. Cartoon of a single pixel of the CIS chip. Metals surround the pixel, thereby making the active pixel a "U" shape.

The dielectric layers are plasma-enhanced chemical vapor deposition (PECVD) low-k (LK) films, which must be etched either using plasma or wet etch processes to open the Si region of the CIS. For this experimental work, the wet etch process has been used to punch through LK, although C_xF_y/Ar-based plasma etch processes can be used and have been tested for feasibility to achieve this. It must be noted that the metals are protected with a LOR formed with a contact mask, as aforementioned and shown in Appendix A, during the lithography process. Due to confidentiality, specific details regarding the LK materials and detailed etch chemistry information are omitted. The etch process was followed by the deposition of Bi_2Te_3 high-Z PAL, which was conducted using a physical vapor deposition (PVD) process such as sputter deposition. The last step of the high-level flow is the photoresist/hardmask stripping process, which is known as the liftoff process if liftoff resist is used. In this step, the remaining layers of materials on top of the photoresist that protect the pixel-surrounding metals and periphery regions were lifted off so that only the pixel-active regions have the high-Z PAL. A complete monolithic PAL-integrated CIS pixel active region prior to wire bonding is shown in Figure 4.
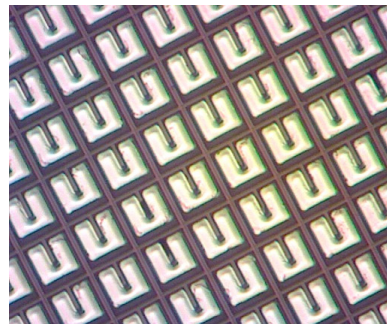
Figure 4. Pixel active region of CIS chip with 250 nm Bi_2Te_3 PAL coverage on each pixel in the "U"-shaped regions after successful liftoff.

In our previous theoretical work, which involved Monte Carlo N-Particle (MCNP) simulations, high-Z PAL was chosen as PbTe [1]. However, it should be noted that due to material unavailability and PVD chamber contamination concerns, another high-Z compound, Bi_2Te_3, which is similar to PbTe, has been chosen to substitute PbTe experimentally. To confirm whether Bi_2Te_3 can be an appropriate substitute for PbTe, the QY enhancement performance of Bi_2Te_3 PAL with 5 μm Si compared to Si direct detection via MCNP simulation can be seen in Appendix B as a verification. It should be noted that using a 5 μm-thick Si is appropriate for such confirmation as the typical Si epitaxial layer thickness of CIS chips is 5 μm as the active absorber [5].

3. Experimental Testing of Bi_2Te_3 PAL-Integrated Si CIS for Hard X-ray Detection

After post-processing, responsivity testing of the chips was undergone to determine whether QY or quantum efficiency (QE; the ratio of the mean number of photoelectrons

generated in a pixel to the ideal number of photoelectrons generated by the incident X-ray photons assuming a perfect impact ionization process) enhances like what the computational efforts have predicted. This work was conducted using an X-ray source at the Helena Foundation Junior Laboratory at the Massachusetts Institute of Technology (MIT).

Based on the experimental results, relative QE enhancements were found to be consistent with the computational results presented in [1]. However, absolute QE is not yet available due to the lack of recent calibration, possible photon flux discrepancies, and possible internal radiation damage of the Amersham AMC.2084 variable hard X-ray source utilized for the experimental efforts [6–8]. More rigorous absolute QE measurement with synchrotron X-ray beamline time at the National Laboratories may be necessary in the future. In this section, in addition to discussing the successful preliminary demonstration of relative QE enhancement of PAL-integrated CIS, noise measurements, dark current measurements, and conversion gain measurements are discussed. Furthermore, we will discuss about the challenges posed by variable X-ray sources, including possible inconsistencies in reported flux and radiation damage causing unintended high signals by CIS.

Four processed and wire-bonded CIS chips were picked for experimental testing. The chips with complete wire bonding that have been tested during the experimental efforts are listed in Table 1 with their corresponding IDs. The partial coverage chips are a result of relatively conformal sputtering deposition that led to partially removed PAL regions during liftoff, as described in the previous section. The partial-coverage CIS chips indicate that, eventually, high-Z PAL thin adhesion layer or seed layer solutions may need to be proposed for improved adhesion.

Table 1. List of post-processed CIS chip identification numbers and the pixel active region PAL thicknesses and coverage descriptions used for experimental measurements to verify the signal enhancement of PAL-integrated CIS chips from the Si reference chip.

Chip ID	Bi_2Te_3 PAL Thickness (nm)	Active Pixel Area Coverage (Full or Partial)
4	1000	Partial
9	250	Full
10	500	Partial
11	0	Si reference

3.1. X-ray Measurement Setup for Experimental Verification

The testing setup for X-ray measurements can be seen in Figure 5. A field-programmable gate array (FPGA) board is connected with a few other peripheral boards that allow the CIS chips to be read. The measurements were conducted at the Helena Foundation Junior Laboratory at MIT. The source, Amersham AMC.2084 Am-241 variable X-ray source, has six target materials: copper (Cu), rubidium (Rb), molybdenum (Mo), silver (Ag), barium (Ba), and terbium (Tb). These target materials down-convert higher-energy gamma rays and α particles emitted by Am-241 into lower-energy characteristic X-rays that correspond to the average energies of the emitted photons listed in Table 2 [6,7,9]. Each target material emits K_α and K_β lines as specified in [6,7], where the former is ~5× stronger than the latter. Therefore, Table 2 only lists the energies of the predominant K_α lines. The full spectra of the X-ray emission can be found in [7]. In addition, inevitably and inconveniently, there may also be Np L X-rays with energies between 11.9 keV and 22.2 keV, gamma rays with energies of ~60 keV, and alpha particles with energies of ~6 MeV (as a product of Am-241 radioactive decay) that are emitted from the source. According to the source specifications, the photon emission is highly collimated and limited to a solid angle of 0.5 sr. As shown in Figure 5, the source is typically placed about 4.2 cm away from the chip. The source is secured by a chemistry clamp. Table 2 also shows the reported source flux shown in the specifications and the flux calculated after the high collimation is taken into consideration [6,7]. A caveat of this specification is that "one photon" in the specification sheet could actually be a pulse of multiple photons that results in a single "click" on the

calibration detector due to its limitation in response time. Therefore, corrections are needed to better evaluate the quantum yield of X-ray photon detection.
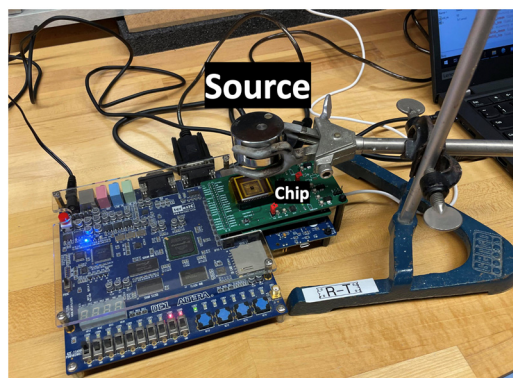
Figure 5. Testing setup for X-ray response measurements.

Table 2. List of target materials, corresponding generated X-ray photon energies (predominantly K_α), and corresponding emitted photon flux of the Amersham AMC.2084 variable X-ray source as reported in the technical specifications. K_β energies can be seen in [6,7], and the intensities are only ~1/5 that of K_α. Photon flux shown in the last column of the Table takes the 0.5 sr solid angle collimation into consideration [6,7].

Target	Average Emitted X-ray Photon Energy—K_α (keV)	# Photons/s/sr (Source Flux)	# Photons/s (Source Flux)
Cu	8.04	2500	1250
Rb	13.37	8800	4400
Mo	17.44	24,000	12,000
Ag	22.1	38,000	19,000
Ba	32.06	46,000	23,000
Tb	44.23	76,000	38,000

It should be noted that there is a glass cover shown on top of the chip in Figure 5. During the measurements, it was realized that the glass cover produces a considerable amount of fluorescence upon X-ray photon excitation. Therefore, the glass cover has been removed for all measurements. In addition, for the QE measurement and determination, which will be discussed later in this section, the source and the chip were covered with Al foil, the entire testing setup was covered by a large cardboard box, and the source-to-sensor distance was set to ~1 cm so that background visible light removal could be maximized.

*3.2. Indication of Photon Energy Down Conversion*

3.2.1. Indication of PEDC via Sporadic Outliers in Conversion Gain

Conversion gain (CG) is a ratio between output and input or a change in output voltage per electron generated by a pixel. Despite the fact that the CIS chips are processed and have PAL films deposited on the pixel active regions, and even though the incident X-ray photon energies are varied, the CG should ideally not change or be very close to the CG prior to the chips being processed unless the capacitance has been altered during the post-processing steps. After characterizing the unprocessed chip, it was found that the CG of the unprocessed chip was 13 $\mu V/e^-$. The CG is calculated using the slope of a mean-variance plot (an example is shown in Figure 6) that represents the overall sensor noise variance, as shown in Equation (1). The calculation involves the pixel output mean values of each image taken from 1 row time (1RT; shortest integration time, which is 61.4 μs) to an extended integration time (couple hundred RT). The readout gain (or readout circuit gain, which was calculated as 0.69 V/V with ±6% change, is determined via analog test mode

transfer function by undergoing a readout linearity measurement with an unprocessed chip). Additionally, the conversion factor of 1 digital number (DN) (signal) is set at 500 μV. Fixed pattern noise, readout temporal noise, and pixel noise measurements for each PAL thickness used in the experiment can be seen in Appendix C.

$$(\text{sensor noise})^2 = (\text{pixel noise})^2 + (\text{readout temporal noise})^2 \tag{1}$$
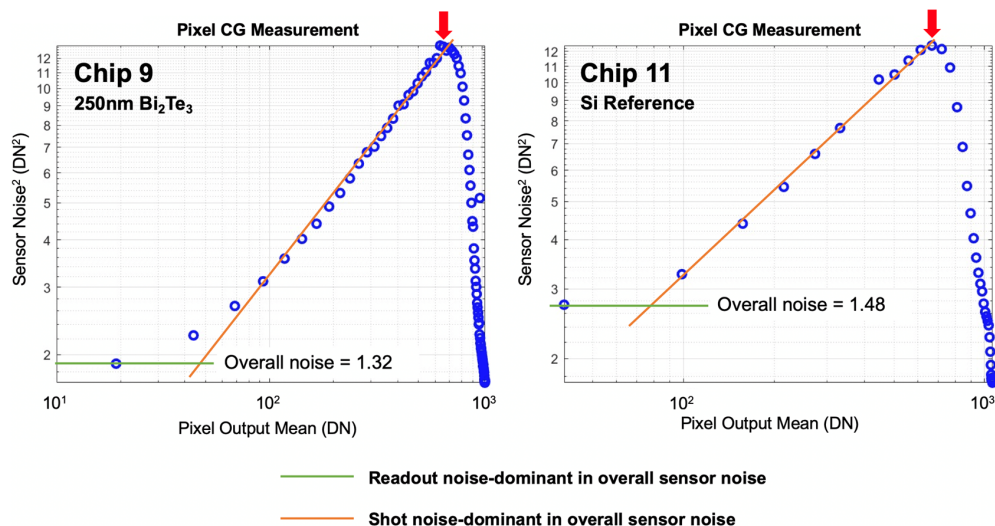

Figure 6. CG measurements of chip #9 (**left**) and chip #11 (**right**) under visible light. Sporadic outliers seen in CG measurements under X-rays are not observed with measurements under visible light. The good linear relationship in the shot noise regime is consistent with the expected Poisson distribution. Red arrows indicate the pixel saturation point. The green horizontal line indicates readout noise dominance in overall noise, and the orange line indicates shot noise dominance in overall sensor noise. Written overall noise values are readout noise-dominant overall noise.

Figure 6 shows the pixel CG measurement for chip #9 and chip #11 under visible light. As aforementioned, these plots compare the square of overall sensor noise (i.e., variance) versus the pixel output mean values. In this case, the curves are smooth, and there are minimal or no sporadic outliers at all. Under visible light, the shot-noise-limited region shows a good linear relation between the variance and the mean output. This is fully consistent with the Poisson distribution of the shot noise, where the variance is proportional to the mean before saturation. The conversion gain can be directly derived from the slope of the linear fit in the shot-noise-limited regime, as mentioned earlier and will be detailed in the later text [10].

However, under incident high-energy X-rays, due to regenerative processes such as impact ionization or avalanche, the distributions of the DNs can be significantly broadened out. This means that the smooth curve can demonstrate extreme deviations, as shown in Figures 7 and 8 [11]. The sporadic outliers in Figures 7 and 8, which will be discussed later in this subsubsection, appear to delineate such widening due to the regenerative processes as shown via the deviations from well-behaved Poisson distributions, and the exact reason behind these outliers must be investigated as a follow-up. Another possible reason behind such a significant broadening of DNs, which may also need to be further investigated in the future, could be the effects of pixel incomplete charge transfer/collection due to the large number of photoelectrons generated by a high-energy X-ray photon. For instance, it is possible that only a fraction of electrons could have been collected by anode pixels, eventually leading to incomplete charge collection events only at edge pixels or sometimes at inter-pixel gaps, causing additional noise [12,13]. InGaP, AlGaAs, and AlInP X-ray photodiodes, although at a larger scale, have incomplete charge collection events that have suffered noise or at least show some degree of what is known as "incomplete charge collection noise" [14,15].
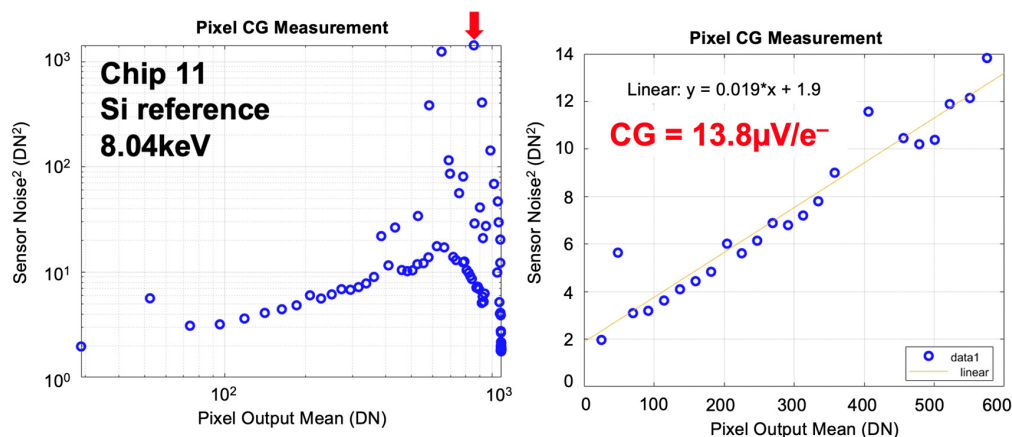
Figure 7. Pixel CG measurement for chip #11, a Si reference chip under 8.04 keV X-ray photon illumination. Using the slope of the linear portion of the plot as shown on the right, the CG is calculated as 13.8 μV/e$^-$. The red arrow indicates the pixel saturation point.
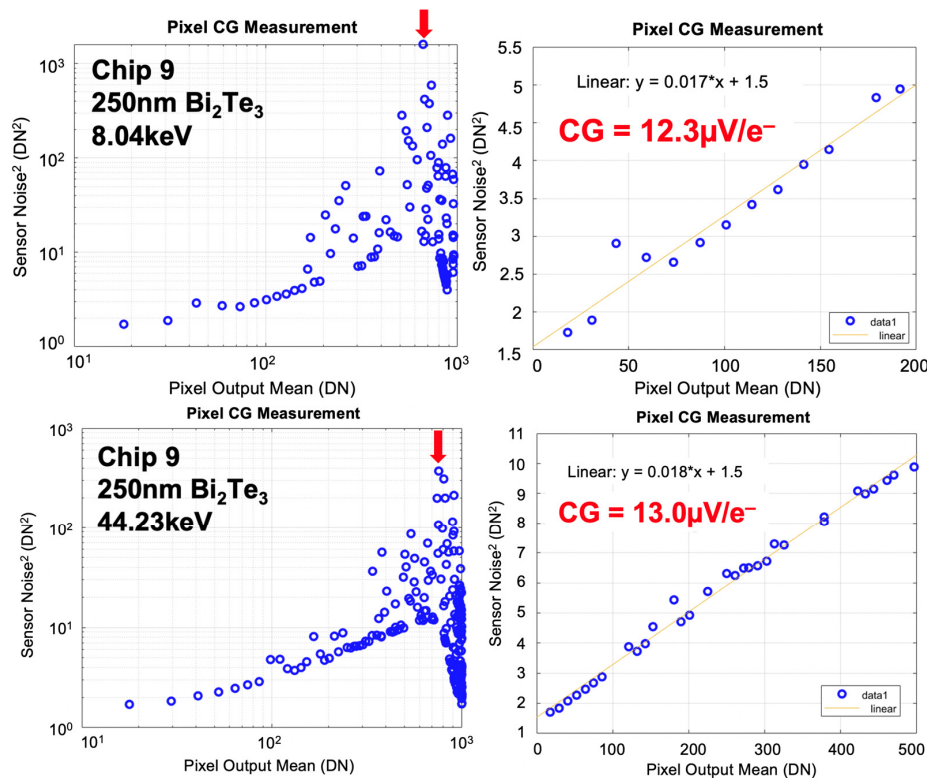
Figure 8. Pixel CG measurement for chip #9, full coverage 250 nm Bi_2Te_3 PAL chip, with 8.04 keV (**top**) and 44.23 keV incident X-ray photon energies (**bottom**). Using the slopes of the linear portions of the plots as shown on the right, the CGs are calculated as 12.3 μV/e$^-$ and 13.0 μV/e$^-$, respectively. Red arrows indicate the pixel saturation point.

Figure 7 shows the pixel CG measurement for chip #11, the Si reference chip, at 8.04 keV incident X-ray photon energy. As aforementioned, this plot compares the square of overall sensor noise (variance) versus the pixel output mean values. Additionally, for the subsequent figures, it should be noted that "data1" with the blue circle in the legend is the measured data, and "linear" with the yellow line is the linear fit performed to determine the slope of the plot prior to saturation. In Figure 8, this legend will be the same. It can be seen from the figure that the slope of the plot prior to saturation is 0.019 DN/e$^-$. The slope is quantified as DN/e$^-$ because sensor noise^2 in the vertical axis, which is the variance, is quantified as $[DN^2/(e^-)^2] \times e^-$ and the pixel output mean in the

horizontal axis is quantified as $(DN/e^-) \times e^-$ [15]. With the readout gain of 0.69 V/V and the aforementioned DN-to-μV conversion factor (1DN = 500 μV), the CG becomes $(0.019\ DN/e^-) \times (500\ \mu V/DN)/0.69 = 13.8\ \mu V/e^-$, which is very similar to the CG of the unprocessed chip (13.2 μV/e$^-$). Therefore, this confirms that CG did not change after the processing steps.

Figure 8 shows pixel CG measurements for chip #9 at 8.04 keV and 44.23 keV incident X-ray photon energies, respectively. Using the slopes of the plots prior to saturation, readout gain, and the DN-to-μV conversion factor, CGs can be calculated as 12.3 μV/e$^-$ and 13.0 μV/e$^-$ for 8.04 keV and 44.23 keV, respectively. Therefore, it can be deduced that the CG does not change for post-processed CIS chips, and the capacitance of the chips is not altered during the post-processing steps. As a result of such a deduction, CGs for other incident X-ray photon energies and chips with different PAL thicknesses and pixel active region coverages were not further measured. In Figure 8, due to the enhanced X-ray PEDC contributed by the PAL layers, there are also a lot more data points significantly deviating from the linear fit line compared to what is shown with the Si direct detection method (unprocessed chip without PAL layer) in Figure 7.

Despite the CG remaining almost identical to that of the unprocessed chip under X-ray illumination, the sporadic outliers shown in Figures 7 and 8 are interesting and unusual features, as those outliers indicate high standard deviations amongst the pixel output values. While the CG remains similar under incident X-ray as expected, Figures 7 and 8 show higher DNs compared to Figure 6 under visible light. There is also a group of data points with a much larger standard deviation than the linear part at lower DNs, in contrast to the CG measurement plots under visible light illumination shown in Figure 6 with smooth curves. Therefore, the outliers from Figures 7 and 8 are indeed due to photomultiplication, so the data points are scattered out. This means that different energy-down conversion processes of high-energy X-ray photons and photoelectrons broaden the distribution of DNs.

3.2.2. Capturing PEDC during Photon Detection Events

It has eventually been realized that the variable X-ray source emits photons in pulses, contrary to the belief that the emission is constant via continuous decay. When images captured at consecutive row times have been subtracted as $N \times RT - (N - 1) \times RT$, RT = 61.4 μs being the row time and N being the total number of RT in the duration of exposure, some of the results were perfectly dark. This darkness indicates no detection event within the corresponding row time interval. On occasion, small and large pulses of absorbed X-ray photons were seen when images at consecutive integration times were subtracted from one another, as shown in Figure 9, with the images detected with PAL-CIS chip #9 at 8.04 keV incident energy. In the figure, the subtraction of images between 47RT and 46RT results in a perfectly dark image without any detection between the two integration times. In sharp contrast, the subtraction of images between 48RT and 47RT indicates a large change, meaning that a pulse of X-ray photons is indeed detected. After this pulse, there are no photons detected between 49RT and 51RT again, similar to the interval between 46RT and 47RT.

X-ray photons being emitted in pulses would mean that once the pixel mean output is plotted as a function of the integration time, there would be steps that would indicate photon pulse detection events. Once the CG measurement data have been plotted so that the pixel mean output would be a function of the integration time, as shown in Figure 10, several small and large steps between consecutive row times along the increasing slopes were observed. An example of this large step can be seen in Figure 10c. It has also been noticed that in some cases, especially closer to the saturation regime, a dip, as shown in Figure 10a, can be observed after the step increase. The exact mechanism should be further investigated in the future, but it could be related to enhanced carrier recombination upon a strong pulse injection of photo-generated carriers.
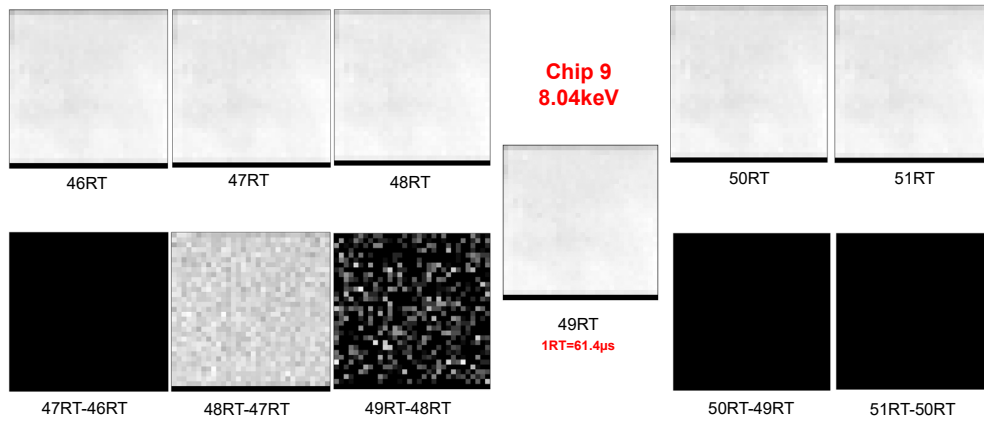
Figure 9. Evolution of photon detection events captured between consecutive row times using chip #9 at 8.04 keV incident energy. The subtraction between images of 48RT and 47RT indicates photon detection activities, while the other subtracted images show little to no photon detection activities, indicating that the X-ray photons from the variable source are emitted in pulses.
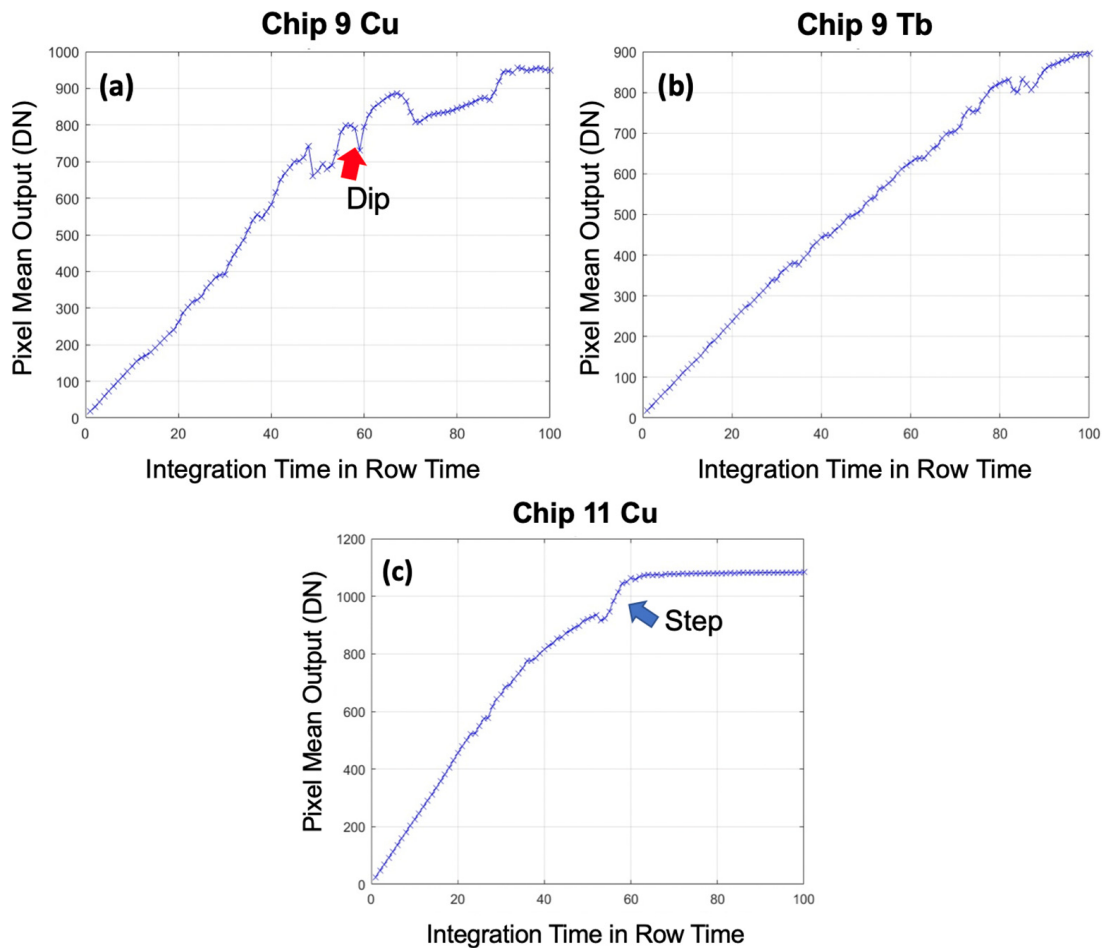
Figure 10. CG measurement data are plotted using pixel mean output as a function of integration time, which is defined as the amount of time that Si CIS (with or without PAL) is exposed to the X-ray source. Small and large steps between consecutive integration times indicate X-ray photon detection events were captured. (**a**) is for chip #9 (PAL-integrated) with 8.04 keV incident energy; (**b**) is for chip #9 with 44.23 keV incident energy; and (**c**) is for chip #11 (reference) with 8.04 keV, where a large step representing photon detection events is indicated with an arrow.

When the images captured at consecutive row times on the said steps are subtracted from one another, images with a large change similar to that of 48RT–47RT shown in Figure 9 can be produced. This means that there are photon pulse detection activities within the corresponding row time interval. Furthermore, when DN or photoelectron counting histograms of the images capturing X-ray detection events are generated (e.g., 48RT–47RT of Figure 9), there are a few (typically >2) distinct Gaussian peaks corresponding to the statistical distribution of the number of photoelectrons detected by the CIS chips. Examples can be seen in Figure 11a–c. The positions of these Gaussian peaks, in DNs, can be converted to the number of electrons using 1DN = 500 µV and the conversion gain of 13 µV/e⁻, i.e., 1DN being equivalent to 500 µV/(13 µV/e⁻) = 38.5 photoelectrons. If these values are multiplied by 3.65 eV, which is the average energy required to create an EHP in Si via impact ionization as described in [1], the most probable estimates of average photon energies down-converted via Bi_2Te_3 PAL can be determined. Using this approach, Table 3 summarizes the distinct peak positions and the down-converted photon energies calculated from the peak positions. For example, in Figure 11a, the first peak is at DN~20. This would correspond to an absorbed photon energy of 20 × 38.5 × 3.65 = 2.8 keV. For the case of chip 11, images from consecutive integration times were not subtracted, but images that are 5RT apart at 58RT and 53RT were subtracted to observe the large step shown with an arrow in Figure 10c of about ~150 DN/pixel as the photon detection events seem to occur over the entire 5RT (~307 µs) rather than over consecutive integration times with a small step. In this jump, three distinct Gaussian peaks are observed, as shown in Figure 11c.
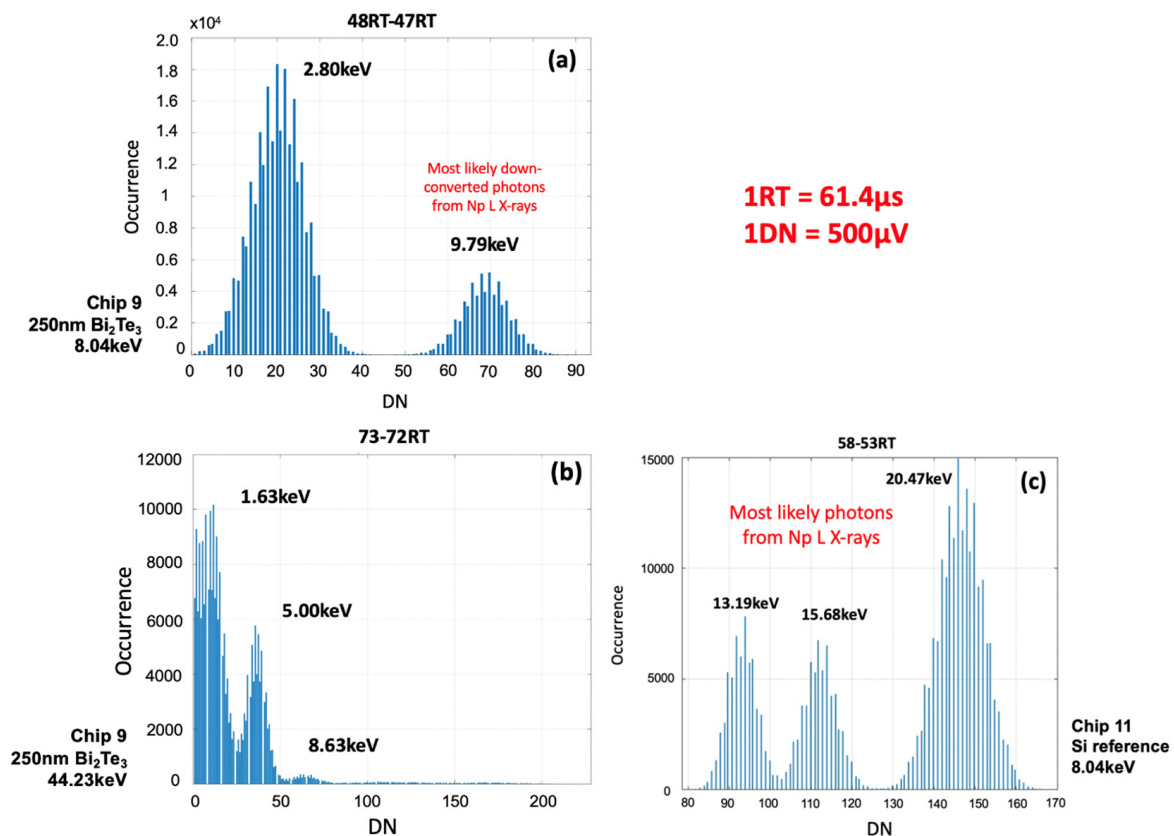
Figure 11. Distinct Gaussians of the image subtractions between (**a**,**b**) consecutive integration times indicated by the steps shown in Figure 10 for chip #9 with 8.04 keV and 44.23 keV incident energies, respectively, and (**c**) 58RT and 53RT for chip #11 with 8.04 keV incident energy. Further details corresponding to the figure are summarized in Table 3.

Table 3. Summary of the photon energies calculated from the photon detection activities between certain integration times that are shown as steps in Figure 10. The peak positions are from the distinct Gaussians shown in Figure 11.

Plot from Figure 11	Gaussian Peak #	Incident Photon Energy (keV)	Subtracted Integration Times (RT; 1RT = 61.4 µs)	Peak Position	# of Electrons	Photon Energy (keV)
(a)	1	8.04	48–47	19.98	7689	2.80
	2			69.74	2682	9.79
(b)	1	44.23	73–72	11.58	445	1.63
	2			35.62	1370	5.00
	3			61.45	2364	8.63
(c)	1	8.04	58–53	145.8	5608	20.47
	2			111.7	4296	15.68
	3			93.93	3613	13.19

The last column of Table 3 summarizes that during the photon detection activities, the incident photon energies are well down-converted. In the case of Figure 11b, with 44.23 keV, the photon energy down conversion is dramatic with 250 nm Bi_2Te_3 PAL as the photons down-convert to 1.63–8.63 keV. While the incident K_α photon energy is 8.04 keV for Figure 11a,c, it can be seen from Table 3 that the photon energies derived from the second Gaussian peak position in Figure 11a and all peaks in Figure 11c are actually higher than the incident photon energy, even considering the K_β photon energy = 8.9 keV [6,7]. As mentioned earlier, the source specifically and inevitably emits Np L X-rays with energies between 11.9 keV and 22.2 keV regardless of the target material [6,7,9,16]. Therefore, photons with energies detected in the case of Figure 11c are most likely photons from such inevitable emission, and the second Gaussian peak from Figure 11a is also most likely the down-converted photon energy from this unavoidable Np L X-ray emission mentioned earlier in the section.

3.3. PAL-CIS Signal Enhancement vs. Si Direct Detection

The pixel output enhancement, or the signal enhancement, of PAL-integrated CIS chips relative to that of Si direct detection should ideally be determined by observing the DN increase in the images taken using PAL-integrated CIS chips compared to those taken using a Si reference chip. A qualitative example can be seen in Figure 12, where (a) shows the image taken with chip #11, the Si reference chip, at 5RT. Additionally, (b) shows the image taken with chip #9, the full coverage 250 nm Bi_2Te_3 PAL chip, under the same condition in the same greyscale for 44.23 keV X-ray photon illumination from the Tb target. Clearly, the chip with the PAL layer shows much higher brightness compared to the Si reference, indicating a strongly enhanced quantum yield of photoelectrons.
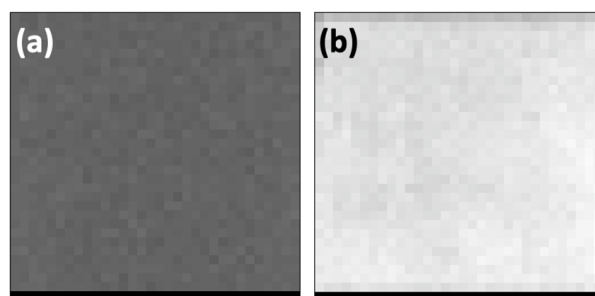
Figure 12. (**a**) Images at 5RT were taken with chip #11, and (**b**) with chip #9 with a 44.23 keV Tb target. Both images are in the same greyscale.

As discussed earlier in this section, the exact incident X-ray photon energy spectrum is not truly monochromatic, despite the fact that the target material mainly produces 44.23 keV X-ray photons. Therefore, strictly speaking, the comparison is not solely due to the QY enhancement in absorbing 44.23 keV X-ray photons. Regardless, it can be seen from Figure 12 that there is a clear qualitative enhancement of PAL-integrated CIS chip #9 from Si reference chip #11.

The best method to quantitatively determine the amount of enhancement of PAL-integrated CIS chips from the Si reference chip was to determine the change in pixel mean output over the change in the integration time (or denoted as the "slope" from here on out). This slope is also directly proportional to the photocurrent generated. Because the measurements inevitably had to be taken in a shared lab setting where visible light exposure was relatively considerable, background measurements without the X-ray source had to be initially taken. The slopes determined with the background measurements were subtracted from the slopes determined with incident X-ray exposures. It should be noted that even though the testing setup is identical to what is shown in Figure 5, the surrounding atmosphere was physically covered. The distance between the X-ray source and the chips was decreased to a minimal level so that the exposure to ambient light could have been minimized.

Table 4 shows complete data on slope measurements of chips #4, 9, 10, and 11, as well as relative signal enhancement of Bi_2Te_3 PAL-integrated CIS chips from the Si reference chip. Figure 13 further visualizes the signal enhancement factors from Si as a function of incident X-ray photon energies for different thicknesses of PAL. The signal enhancement factor is calculated using Equation (2).

$$\text{enhancement factor} = \frac{\text{slope of PAL integrated chips}}{\text{slope of Si reference chip}} \qquad (2)$$
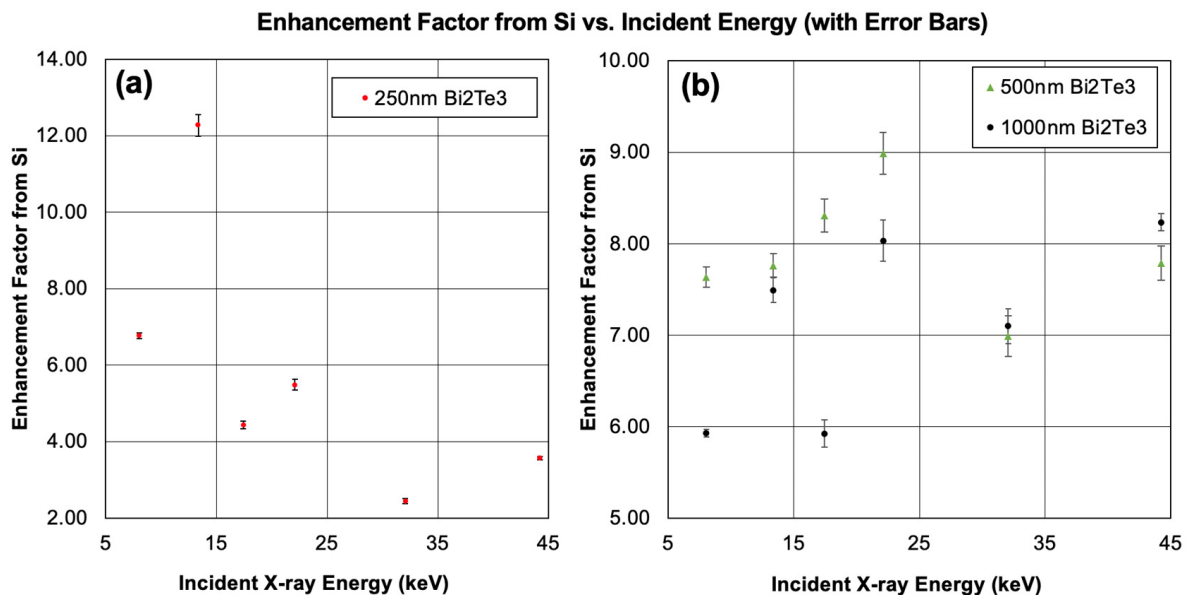
Figure 13. (**a**) Enhancement factor from Si as a function of incident X-ray photon energy for 250 nm Bi_2Te_3 PAL thickness with error bars and (**b**) for 500 nm and 1000 nm Bi_2Te_3 PAL thicknesses as seen in Table 4. The error bars are within the marker size due to the small error propagation (Table 4's last column shows the corresponding error propagation).

Table 4. Summary of complete data on the slopes of chips #4, 9, 10, and 11 and the relative signal enhancement of Bi_2Te_3 PAL-integrated CIS chips from the Si reference chip. Corresponding propagations are shown for the slope measurements and the enhancement factors from Si.

Chip #	PAL Thickness (nm)	Incident Energy (kev)	Background Slope (dDN/dRT)	Measured Slope (dDN/dRT)	Difference (dDN/dRT)	Enhancement Factor from Si
11	0	8.04	5.83 ± 0.02	11.21 ± 0.01	5.38 ± 0.02	Si Reference
		13.37		9.81 ± 0.05	3.98 ± 0.05	
		17.44		11.62 ± 0.11	5.79 ± 0.11	
		22.1		10.4 ± 0.11	4.57 ± 0.11	
		32.06		12.02 ± 0.16	6.19 ± 0.16	
		44.23		11.71 ± 0.03	5.88 ± 0.04	
9	250	8.04	10.24 ± 0.17	46.68 ± 0.33	36.44 ± 0.37	6.77 ± 0.07
		13.37		59.07 ± 0.86	48.83 ± 0.88	12.27 ± 0.28
		17.44		35.93 ± 0.16	25.69 ± 0.23	4.44 ± 0.09
		22.1		35.32 ± 0.15	25.08 ± 0.23	5.49 ± 0.14
		32.06		25.39 ± 0.07	15.15 ± 0.18	2.45 ± 0.07
		44.23		31.21 ± 0.11	20.97 ± 0.20	3.57 ± 0.04
10	500	8.04	4.07 ± 0.12	45.15 ± 0.54	41.08 ± 0.55	7.64 ± 0.11
		13.37		34.97 ± 0.27	30.90 ± 0.30	7.76 ± 0.13
		17.44		52.17 ± 0.48	48.10 ± 0.49	8.30 ± 0.18
		22.1		45.14 ± 0.29	41.07 ± 0.31	8.99 ± 0.23
		32.06		47.35 ± 0.80	43.28 ± 0.81	6.99 ± 0.22
		44.23		49.85 ± 1.06	45.78 ± 1.07	7.79 ± 0.19
4	1000	8.04	3.10 ± 0.07	35.01 ± 0.17	31.91 ± 0.18	5.93 ± 0.04
		13.37		32.92 ± 0.34	29.82 ± 0.35	7.49 ± 0.13
		17.44		37.41 ± 0.55	34.31 ± 0.55	5.93 ± 0.15
		22.1		39.81 ± 0.48	36.71 ± 0.49	8.03 ± 0.22
		32.06		47.04 ± 0.23	43.94 ± 0.24	7.10 ± 0.19
		44.23		51.52 ± 0.44	48.42 ± 0.45	8.23 ± 0.09

It should be noted that the slopes indicated in Equation (2) equal the difference between the measured slopes and the background slopes, as shown in the 6th column of Table 4. It can be seen from the table that for lower PAL thickness, the maximum enhancements are at lower energies than 44.23 keV. Furthermore, it can be seen in Figure 13b that the trends of 500 nm and 1 μm Bi_2Te_3 PAL are very similar. This may be because the QY saturates as the PAL thickness goes beyond 500 nm, as reported via MCNP simulation using PbTe PAL in [1]. In Table 4 and Figure 13, propagation of uncertainties (or error propagations) can be seen for enhancement factors along with the slope uncertainties determined via linear regression analysis of the measured slopes, which is necessary to calculate those enhancement factors. As shown in Table 4, the relative error appears to be slightly higher at higher energy photons due to weaker signals. With 1 μm Bi_2Te_3 PAL, the enhancement is maximized at the highest incident photon energy available at the source. In addition, consistent with the results from the computational efforts in the previous work with PbTe PAL [1], the relative enhancement using Bi_2Te_3 PAL from a Si reference chip is 3–12× depending on the PAL thickness and X-ray photon energy. This indicates that the proposed thin high-Z PAL supersedes the Si direct detection method and can be utilized to pave the way toward a new method of high-energy X-ray detection.

3.4. Estimation of Quantum Efficiency of PAL-CIS

Quantum efficiency (QE) calculations were a critical part of the preliminary demonstration of PAL-integrated CIS chips. The QE can be directly compared to the QY results

from our previous work, and verification of consistency was highly necessary. Equation (3), adapted from [17], can be used to calculate the QE.

$$QE = \left[\left(\frac{\Delta DN}{\Delta T_{int}} \right) \times (500 \text{ μV/CG}) \right] / \left[\left(\frac{E}{3.65} \right) \times \Phi \right] \tag{3}$$

In Equation (3), $\frac{\Delta DN}{\Delta T_{int}}$ is the slope after background slope subtraction calculated in the previous subsection (or 6th column of Table 4; ΔT_{int} is the integration time converted from RT to seconds), CG is the conversion gain, E is the incident photon energy, 500 μV is the conversion factor for DN, and Φ is the incident photon flux normalized to the beam area, taking pixel active region area into consideration. All variables and factors must be converted to appropriate SI units.

Source Flux Accuracy Challenges and Calibration

The source flux shown in Table 2 [6] is extremely low. This means that none of the CIS chips, especially the Si reference chip, should have had any sort of signals or pixel outputs during a short exposure time of the sensor to the source, as opposed to the actual experimental results of [4,18] showing clear X-ray photon detection. In addition to this, using exactly the same variable X-ray source, COTS Si CIS-based devices such as the ON Semi Vita 5000, which has about ~4 million pixels, show more than half of the pixels with photon absorption for an incident X-ray photon energy of 8.04 keV [4]. For 8.04 keV incident energy, with 1250 photons/sec in Table 2 and taking the normalization to the beam area (125.66 mm^2) and the pixel area of the ON Semi Vita 5000 (4.8 × 4.8 μm^2, 2059 × 2048 pixels) into consideration, the flux hitting the pixel active region of this COTS CIS device would be 1216.64 photons/s [19]. The authors of [4] claim that the exposure time was approximately 30 s, meaning that no more than 1% of the ~4 million pixels on the device should output signals under 8.04 keV X-ray illumination, rather than half the pixels observed experimentally. The actual observation would require an X-ray photon flux on the order of mid 10^4 photons/sec. Therefore, this is a possible indication of inaccurate source flux reported by the technical specifications [6,7]. It is also possible that the source specifications counted each pulse of photons as one photon, as discussed earlier. This would lead to significantly underestimating the flux, as each pulse could have numerous photons. Furthermore, the technical specifications and the reported flux have not been independently verified for over 50 years since their creation.

In addition to the highly probable discrepancy in photon flux, another possibility of strong signals by purely Si-based devices without PAL might be the existence of Np L X-rays (11.9–22.2 keV) and low energy gamma rays (~60 keV) from the Am-241 variable X-ray source, as well as alpha particle (~6 MeV) emission via an inevitable alpha decay [6]. The reported emissions spectrum of the source via a spectrometer indicates a low-energy gamma-ray emission at around 60 keV, superseding the intensity of target materials in the source that create lower hard X-rays below 60 keV [6,16]. Moreover, specs define the lifetime of the source as 15 years, which is merely a fraction of the 432-year half-life of Am-241 [7]. Most of the in-commission Am-241 variable X-ray sources are over a couple of decades old. The source utilized for this work is about five decades old. The alpha particles released from the decay of Am-241 are of very high energy, as previously stated. This would have introduced radiation damage to the target materials over the past five decades, causing vacancies and voids, allowing more high-energy particles to pass through, and reducing the efficiency of X-ray generations. The efficacy reduction may be why the source lifetime is defined as 15 years in the first place. The emissions of gamma rays and alpha particles may also have a high flux.

Due to these discrepancies, the true source flux for each energy and the true incident photon energies are unknown, given the inevitable Np L X-ray, gamma ray, and alpha particle emissions. Therefore, it is not possible to directly determine the QE. Eventually, for future evaluations, to know the true radiation spectra of the source and the target metals, semiconductor detectors (e.g., Ge-SSD), which can provide spectra rapidly and

cost-effectively, should be used for better accuracy [20]. In the interim, however, assuming that QY produced in MCNP without PAL in our previous work [1] is an ideal QY = QE scenario, where the incident photons absorbed by Si completely transfer their energies to primary photoelectrons and perfect impact ionization occurs, the actual photon flux at 8.04 keV can be determined by "reverse engineering" using Equation (3). All the other variables in the equation are measured or determined by MCNP (QE only). For 8.04 keV using a Si reference design without PAL, this is a reasonable assumption since the Beer's Law comparison with MCNP output was very consistent, as shown in Figure A3 of [1]. Then, something close to the real photon flux at 8.04 keV can be determined. It should be noted that the reported typical Si epi layer thickness on the CIS chips used for this work is 5 μm [2]. The Si substrate, which is usually around several hundred μm in modern CIS with Si epi layers, typically uses heavy p+ doping for epitaxial growth to deliberately reduce carrier diffusion from the substrate to epi layers [21,22]. Due to the insignificant lifetime of charge carriers, the substrate will not be considered a detector active region, as such a region will be limited to the depths of the Si epi layer [21]. Therefore, for the "reverse engineering" steps, QY determined with 5 μm Si and 8.04 keV incident X-ray photon energy can be used. Using this "real" flux, a scaling factor can be calculated using the reported source flux shown in Table 2, since the main issue with the original flux data is the confusion between a single photon and a pulse of photons based on our discovery in Figures 9 and 10. With this calibration, the flux of 8.04 keV photons is also much more consistent with the actual observations in [4,11], as discussed earlier. This scaling factor can be utilized to calibrate the other reported source fluxes for other incident energies. The scaling factor was calculated to be about 27. Table 5 shows the list of calibrated source fluxes from the reported flux using the scaling factor.

Table 5. Summary of calibrated flux, determined by scaling factor after using theoretical QY output by MCNP, corresponding to each incident energy of the Amersham AMC.2084 variable X-ray source. Assuming that MCNP outputs the correct theoretical QY with an ideal QY = QE scenario at 8.04 keV with 5 μm Si, using the reverse engineering method to determine scaling factors and flux listed on the Table should lead to a set of calibrated fluxes that are close to the real flux of photons emitted by the source.

Incident Energy (keV)	Original Flux (Photons/s)	Calibrated Flux (Photons/s)
8.04	1250	3.40×10^4
13.37	4400	1.20×10^5
17.44	12,000	3.26×10^5
22.1	19,000	5.16×10^5
32.06	23,000	6.25×10^5
44.23	38,000	1.03×10^6

Using the calibrated flux, a more accurately estimated QE can be seen in Figure 14. We stress that this is an educated estimate of QE in terms of order of magnitude, limited by the uncertainties in the X-ray source. At the same time, the key point is actually the relative enhancement due to PAL discussed in Figure 13. In the figure, we also show a comparison between QE determined with the calibrated flux and simulated theoretical QE values by MCNP. For the latter case, the QE enhancement factor up to $4\times$ from Si direct detection can be calculated. It should be noted that the theoretical QE values for the cases with PAL are lower than QY, as down-converted photons are taken into consideration for the calculation, ultimately leading to fewer secondary photoelectrons after impact ionization due to lower photon energies absorbed by Si. Additionally, (EXP) in the figure stands for experimental measurements (or, in this case, QE evaluated via the aforementioned reverse engineering steps and calibration), and (SIM) stands for simulated results using different thicknesses of Bi_2Te_3 PAL and 5 μm Si between 8.04 keV and 44.23 keV incident X-ray photon energies.
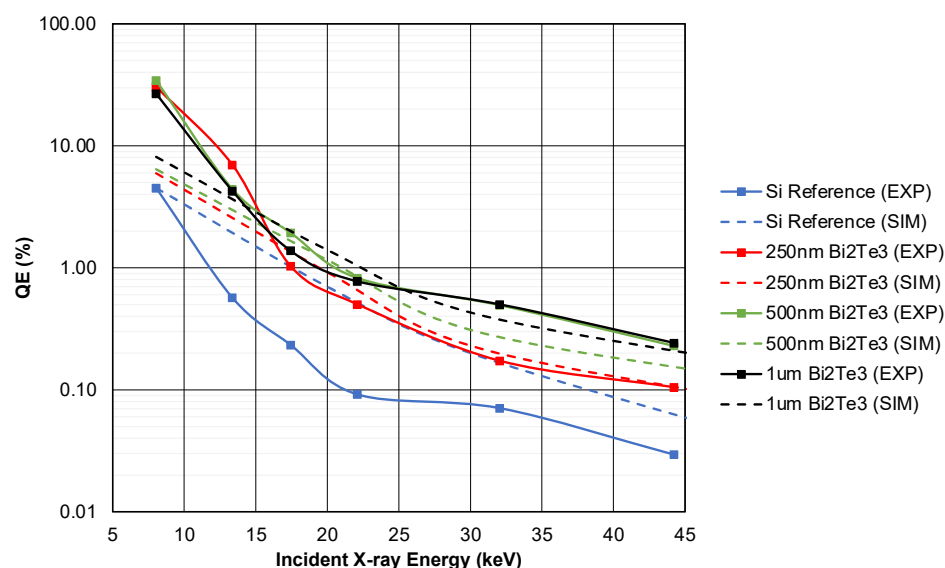
Figure 14. Experimental or calibrated QE (EXP) and simulated QE (SIM) for 250 nm, 500 nm, 1 μm Bi$_2$Te$_3$ PAL, and 5 μm Si.

Overall, the experimental and simulated QEs semi-quantitatively agree with each other, showing better consistency, especially for PAL-integrated CIS at >15 keV X-ray photon energy. Some discrepancy is understandable, considering the uncertainty in X-ray flux calibration. Measured QE, especially for a Si reference chip with no PAL, may also be lower than QY (ideal QE) in reality due to energy loss from processes upon impact ionization and energy transfer from photons to electrons. On the other hand, the relative enhancement of measured QE still remains the same, as shown in the second-to-last column in Table 4. Additionally, the QE enhancement effect introduced by PAL has been experimentally confirmed. The several measured QE enhancement factors from Si are above the theoretical QE enhancement factor prediction of up to 8–10×. Some measured QE enhancement factors are consistent with the 8–10× enhancement prediction. Absolute QE using synchrotron X-ray sources should be determined in future work.

4. Comparative Studies of PEDC in Different PAL and Scintillator Materials

A follow-up study was conducted to investigate and compare the PEDC performance of high-Z PAL Si CIS vs. lower-Z PAL material and commonly used scintillator material. To this end, experiments were conducted to assess the performances of five Si CIS configurations that varied according to whether the device included a high-Z PAL, 250 nm Bi$_2$Te$_3$, a lower-Z substitution material, 500 nm Sn, a conventional scintillator material, L$_2$Y$_2$SiO$_5$ (LYSO) [23,24], and incidentally, a PMMA window. While high-Z PAL-CIS has been experimentally verified as a powerful tool to enhance QE compared to Si direct detection, another necessary verification was to determine whether coupling high-Z PAL with conventional state-of-the-art scintillator materials such as LYSO or materials that have been proven to assist with a light extraction efficiency enhancement would help with further increase in QE [25–27]. The specifications for each of the five treatments in the follow-up study are tabulated in Table 6. The components of each treatment setup were positioned in the following order from the top (e.g., closest to the X-ray source) to the bottom (e.g., closest to the Si chip housing on the FPGA board, which rested on the lab bench): 0.5 mm-thick LYSO scintillator; 3 mm-thick PMMA window; unmeasured but approximately 2 mm of air gap; 250 nm Bi$_2$Te$_3$ PAL; 500 nm Sn; and Si chip. The PAL and Sn components were layers of material deposited onto the Si chips and thus are always found at the bottom end of this order. The air gap and the PMMA window existed to protect the fragile chip packaging, including from contact with the LYSO scintillator.

Table 6. Follow-up comparative study treatments. Components are tabulated in the center of five columns from left to right in descending order of proximity to the X-ray source.

Treatment	LYSO Scintillator	PMMA Window	250 nm Bi$_2$Te$_3$ PAL	500 nm Sn	Si	Chip ID
A	No	Yes	No	Yes	Yes	3
B	Yes	Yes	No	Yes	Yes	3
C	No	No	Yes	No	Yes	9
D	No	Yes	Yes	No	Yes	9
E	Yes	Yes	Yes	No	Yes	9

This study introduced two key improvements over prior investigations. First, the physical setup of the experiment was more tightly controlled to significantly reduce background noise. Second, new signal processing algorithms were developed and employed to perform several tasks: (1) filter, identify, evaluate, and record individual X-ray detection events from the raw device output signal; (2) compute and record the photoelectron counts that were generated by each X-ray detection event; and (3) filter, identify, evaluate, and record pixel crosstalk events. With these improvements, this study ultimately further supported the results that were reported in the previous section.

4.1. X-ray Detection Event and Pixel Crosstalk Processing Algorithms

The X-ray detection event processing algorithm functioned as follows: For each pair of consecutive frames of readout signal data adjusted by fixed pixel noise $f - 1$ and f, the X-ray detection event processing algorithm computed the change in DN value ΔDN for each pixel (x, y).

$$\Delta DN(x, y, f) = DN(x, y, f) - DN(x, y, f - 1) \tag{4}$$

A given pixel is considered to be the site of an X-ray detection event at the time that corresponds to the second frame if and only if its change in DN value from the first frame to the second frame is greater than a threshold value θ_{DN}. When a frame's pixel qualifies as the site of an X-ray detection event, its change in DN value is added to the value of the corresponding pixel of an X-ray detection event DN difference sum matrix Δ (Equations (5) and (6)), and 1 is added to the value of the corresponding pixel of an X-ray detection event count matrix M (Equations (7) and (8)).

$$\delta(x, y, f) = \begin{cases} \Delta DN(x, y, f), & \text{if } \Delta DN(x, y, f) > \theta_{DN}; \\ 0, & \text{otherwise.} \end{cases} \tag{5}$$

$$\Delta(x, y) = \sum_{f \in F} \delta(x, y, f) \tag{6}$$

$$m(x, y, f) = \begin{cases} 1, & \text{if } \Delta DN(x, y, f) > \theta_{DN}; \\ 0, & \text{otherwise.} \end{cases} \tag{7}$$

$$M(x, y) = \sum_{f \in F} m(x, y, f) \tag{8}$$

The algorithm also computes the number of photoelectrons generated by the detection event n via the conversion gain CG (Equation (9)) and adds it to the value of the corresponding pixel of an X-ray detection event-generated photoelectron count sum matrix N (Equation (10)).

$$n(x, y, f) = \begin{cases} \left\lfloor \frac{500 \ \mu\text{V·DN}^{-1}}{CG} \Delta DN(x, y, f) \right\rfloor, & \text{if } \Delta DN(x, y, f) > \theta_{DN}; \\ 0, & \text{otherwise.} \end{cases} \tag{9}$$

$$N(x, y) = \sum_{f \in F} n(x, y, f) \tag{10}$$

The frame-to-next-frame change in DN value threshold value of θ_{DN} should be chosen such that a frame-to-next-frame change in DN value greater than θ_{DN} is never expected to be observed unless an X-ray detection event has occurred. To minimize the number of X-ray detection events that the algorithm excludes, the least of all valid θ_{DN} values for which this condition experimentally holds true should be chosen. For the sake of practicality, this definition is approximated by another definition: θ_{DN} is the greatest change in DN value that is expected to be observed in the absence of any X-ray detection events. θ_{DN} was experimentally defined as the greatest of the changes in DN value that were observed for any of the conditions that were excluded from exposure to the X-ray source. The θ_{DN} for the follow-up study was experimentally determined according to this definition to be 10DN.

A second algorithm was developed to discern, evaluate, count, and report "pixel crosstalk events." These are occasions on which incident X-ray photons and/or down-converted photons collide with the non-sensing border between two or more pixels. Pixel crosstalk events are indicated by two or more adjacent simultaneous X-ray detection events. The pixel crosstalk processing algorithm discerned pixel crosstalk events from the fixed pixel noise-adjusted readout signal data in a manner similar to the X-ray detection event processing algorithm, but it discarded X-ray detection events for which no simultaneous X-ray detection events were observed in any adjacent pixels and duplicated. The pixel crosstalk processing algorithm borrowed from and adapted sub-algorithms developed for the X-ray detection event processing algorithm. It was modified to produce single-frame matrices and sum matrices analogous to those produced by the X-ray detection event processing algorithm. The pixel crosstalk event counts were used to adjust and inform analyses of the outputs of the X-ray detection event processing algorithm.

The pixel crosstalk processing algorithm found 14 pixel crosstalk events for Treatment C, 9 for Treatment D, and 0 for Treatments A, B, and E, all under 22.1 keV X-ray photon excitation. Interestingly, the pixel crosstalk processing algorithm found a pixel crosstalk event that spanned three or four adjacent pixels within Treatment D's data. A visualization of this several-pixel detection event anomaly and a visualization of the primary proposed interpretation are depicted in Figure 15. It also depicts visualizations of detected pixel crosstalk events from Treatments C and D.
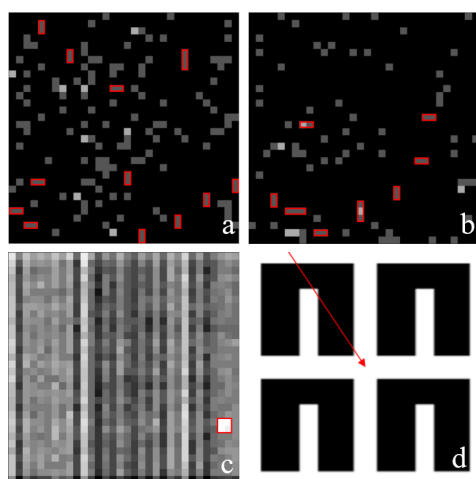
Figure 15. Visualizations of detected pixel crosstalk events. Visualizations of raw X-ray detection event count matrices M (Equations (7) and (8)) with a linearly increasing brightness scale from 0 to 2 X-ray detection events and sites of pixel crosstalk events outlined in red for (**a**) Treatment C and (**b**) Treatment D. (**c**) Visualization of the raw signal at frame 213 of stack 38 of Treatment D's raw data, with an anomalous several-pixel crosstalk event outlined in red. (**d**) Artistic representation of the primary proposed explanation of the anomalous several-pixel crosstalk event: A 6.30 keV X-ray (red arrow) photon was incident on the border crossroads at the center of four adjacent pixels.

4.2. Results: Count Matrices and PEDC Performance Metrics

Generated photoelectron and raw X-ray detection event count matrices from the follow-up study are visualized in Figure 16. Clearly, high-Z Bi$_2$Te$_3$ PAL in treatments C and D without the LYSO scintillator produced the most detection events, as expected.
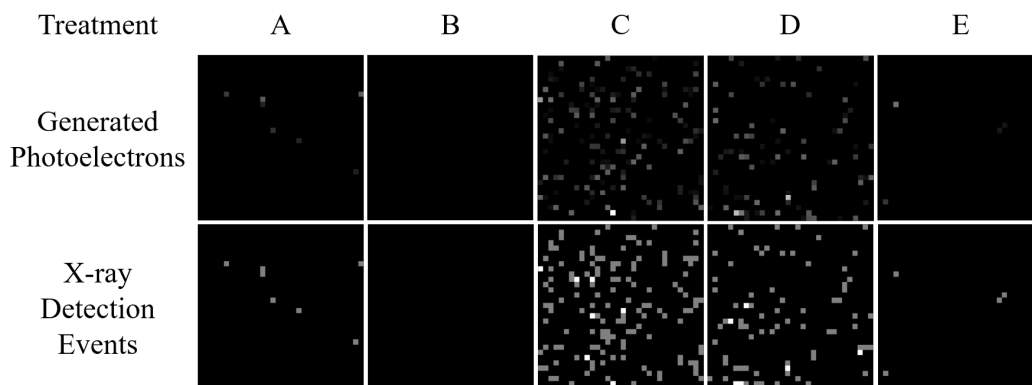
Figure 16. Visualizations of generated photoelectron count matrices ("Generated Photoelectron" row) and raw X-ray detection event count matrices ("X-ray Detection Events" row) by treatment ("Treatment" row). The incident X-ray photon energy is 22.1 keV. The brightness scale of each of the generated photoelectron count matrix visualizations is linear and ranges from 0 photoelectrons (black, 0 brightness) to 5830 photoelectrons (white, 255 brightness). The generated photoelectron count matrix visualizations would appear identical to the aggregated detection event intensity matrix visualizations for the respective treatments, but each with an otherwise identical brightness scale that ranges from 0 DN to 295 DN. The brightness scale of each of the raw X-ray detection event count matrix visualizations is linear and ranges from 0 X-ray detection events (black, 0 brightness) to 2 X-ray detection events (white, 255 brightness).

Results from the follow-up study that are relevant to assessments of PEDC performance are tabulated in Table 7. The QE values of these results were calculated once from Equation (3) and separately from Equation (11), which adapts Equation (3) to leverage algorithm-generated photoelectron counts *PE*.

$$\text{QE} = \left[\frac{PE}{\Delta T_{int}} \right] / \left[\left(\frac{E}{3.65} \right) \times \Phi \right] \tag{11}$$

Table 7. Follow-up study results on the QE of detecting 22.1 keV X-ray photons. Values in the "Adjusted Total Count, X-ray Detection Events" column represent the detected incident X-ray photon counts, which are derived by adjusting the respective raw X-ray detection event counts—which are not included in the table—to account for multiply-counted detected incident X-ray photons as indicated by pixel crosstalk events.

Treatment	Adjusted Total Count, X-ray Detection Events	Total Count, Generated Photoelectrons	QE via Equation (3) (%)	QE via Equation (11) (%)
A	10	1744	0.232	0.038
B	0	0	−0.015	0
C	138	158,994	0.907	3.48
D	79	104,919	2.47	2.30
E	4	4711	0.69	0.10

4.3. Summary of Comparative Studies of PAL

The results of the follow-up study fully support two hypotheses:

(1) Bi_2Te_3 makes for a better-performing PAL material than the lower-Z Sn.
(2) Pairing a Bi_2Te_3 PAL—and possibly Sn as well—enhanced the X-ray detection of Si CIS, while further coupling with conventional scintillator material LYSO reduced its performance.

The results support hypotheses (1) and (2) regardless of which QE calculation method is used. Taking the fully supported hypotheses (1) and (2) together, the results of the follow-up study support the hypothesis that monolithic integration of high-Z Bi_2Te_3 PAL on Si CIS is the most effective method to detect hard X-rays between 20 keV and 50 keV as opposed to the lower-Z Sn or coupling with the conventional scintillator material LYSO.

4.4. Photon Energy Distribution Histogram Comparison

In [1], X-ray photon energy distribution histograms have been reported. The detected photon energy distributions for Treatments C and D in the follow-up study closely matched the expected distributions for a PbTe-Si CIS detector chip, as predicted by MCNP simulations. This alignment suggests that the performance of the PbTe-Si CIS detector chip is not expected to deviate significantly from that of a Bi_2Te_3 PAL-Si CIS chip.

The detected photon energy distribution histograms for Treatments C and D could be made more accurate by accounting for pixel crosstalk and pixels at which multiple events occurred. To account for pixel crosstalk, the datapoints for which the pixel crosstalk events were responsible should first be removed from the datasets. For each of the two treatments, the datapoints that correspond to each pixel crosstalk event should be summed to produce one datapoint per one-pixel crosstalk event. These sets of datapoints should then be reintroduced to the histogram datasets. To account for the pixels at which multiple events occurred, the datapoints that correspond to pixels at which multiple X-ray detection events occurred should each be dissolved into a set of datapoints that each correspond to one of the constituent X-ray detection events.

Figure 17 shows the photon energy histograms of Treatments C and D alongside the MCNP-predicted photon energy distribution histogram for a PbTe PAL-enhanced Si CIS detector chip exposed to incident photons with energies of 20 keV. Notable features include peaks at ~7.86 keV on both treatments' histograms that approximately correspond to the L_3 edge (Pb) peak on the PbTe distribution and peaks at low energies on both treatments' histograms and the PbTe distribution. The deviation is due to the fact that we used Bi_2Te_3 experimentally, and Bi has a slightly higher energy of X-ray absorption edges compared to Pb, which is a heavier adjacent element in the periodic table. Additional corresponding features are indicated with red arrows in Figure 17. Figure 17 compares a simulated photon energy distribution for a PbTe device exposed to 20 keV incident photons to measured photon energy histograms for a Bi_2Te_3 device exposed to 22.1 keV incident photons. However, the strong parallels between the distribution and the histograms constitute evidence that the data produced by the X-ray detection event processing algorithm are in accordance with what would be expected of PAL-attenuated X-ray detection.
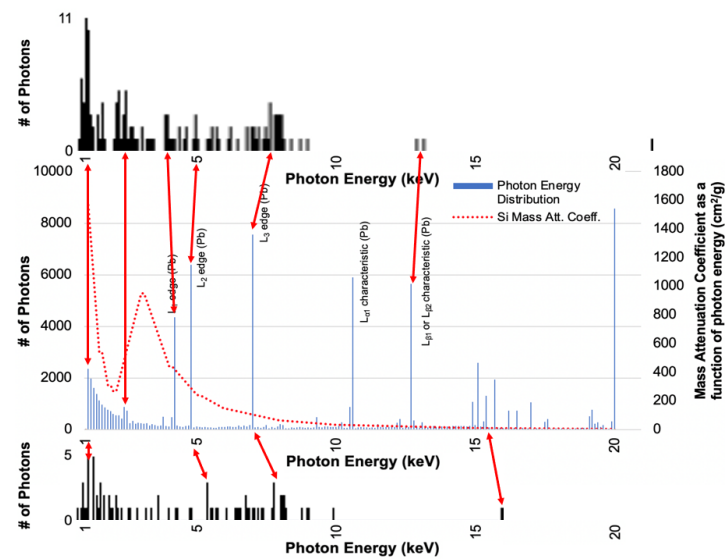
Figure 17. Photon energy histograms from Treatment C's aggregated intensity graph from the new algorithm (**top**), Monte Carlo simulations of a PbTe-on-Si PAL-based X-ray detector under 20 keV incident energy from [1] (**middle**), and from Treatment D's aggregated intensity graph from the new algorithm (**bottom**). All three are on the same energy scale. Red arrows connect similarities between the newly generated histograms and the MCNP photon energy distribution.

5. Concluding Remarks

In our previous work, we introduced a new high-energy X-ray direction concept capable of enhancing the QY by 10–30× for Si-based X-ray detectors using high-Z PAL. This concept has been getting significant attention from the X-ray detector community as it could be a solution to long-lasting efficiency issues with existing Si CCD, photocathode, and scintillation methods. To promote even more confidence in this concept, experimental verification of [1] was presented in this work. Process integration steps to monolithically integrate PAL layers on Si CIS were demonstrated, and experimental verification and associated measurements of efficient photon-to-electron conversion via high-Z Bi_2Te_3 PAL were presented. Most importantly, qualitative signal enhancement and QE enhancement of 3–12× have been demonstrated and validated with consistency. Additionally, new algorithms have been developed to further improve the PAL-CIS measurements with greater accuracy and precision. Although further improvements and enhancements need to be made in terms of cleanroom process stability, PAL-CIS chip yield rate, choice of incident X-ray source, and ambient light control, the PEDC effect from high-Z PAL layers was confirmed with this experimental study. In the future, if these improvements are made in these areas, results with further improved accuracy may be produced.

In the presented work, an Amersham AMC.2084 variable hard X-ray source has been utilized. However, due to the aforementioned reliability issues and the maturity of the source, the validity of the results is more challenging. In the ideal scenario, the measurements should be taken at single-energy synchrotron beamlines such as the Advanced Photon Sources (APS) at Argonne National Laboratory [28,29] or beamline measurements at other synchrotron facilities (e.g., National Synchrotron Light Source II at Brookhaven National Laboratory) [30]. These facilities would provide more accurate and reliable QE results for comparison with the simulated and experimental results presented in this work. Future follow-up works are planned to undergo such beamline measurements at synchrotron facilities for more accurate and reliable results and to compare them with the results presented in this work. Nevertheless, based on the findings presented in this study, the capacity to monolithically integrate PAL on Si CIS and enhance the QE was demonstrated to a sufficient extent such that PAL-enhanced Si CIS should be considered a strong candidate for the next state-of-the-art class of X-ray detection devices, in particular

in next generation X-ray free electron laser light source applications and X-ray camera designs for synchrotrons.

Author Contributions: PAL modeling, process engineering, and experimental verification were performed by E.L. under the supervision of J.L. A follow-up study (algorithm development, algorithmic signal processing, and experimental verification) was performed by K.D.L. under the supervision of J.L. Z.W. provided guidance to E.L. on PAL modeling and to K.D.L. on experimental work. X.Y. designed the CIS chips and contact mask for the process under the supervision of E.R.F. X.Y. and E.R.F. provided guidance throughout the experimental characterization work. The manuscript was prepared by E.L. and K.D.L. under the guidance of J.L. All authors have read and agreed to the published version of the manuscript.

Data Availability Statement: Not applicable.

Conflicts of Interest: The authors declare no conflict of interest.

Appendix A

Figure A1 shows the schematic of the entire contact mask designed and utilized for photolithography to protect non-pixel active regions of the CIS chip. Each square in the figure represents pixel active regions that need to be covered during exposure using negative-tone LOR for the lithography process.
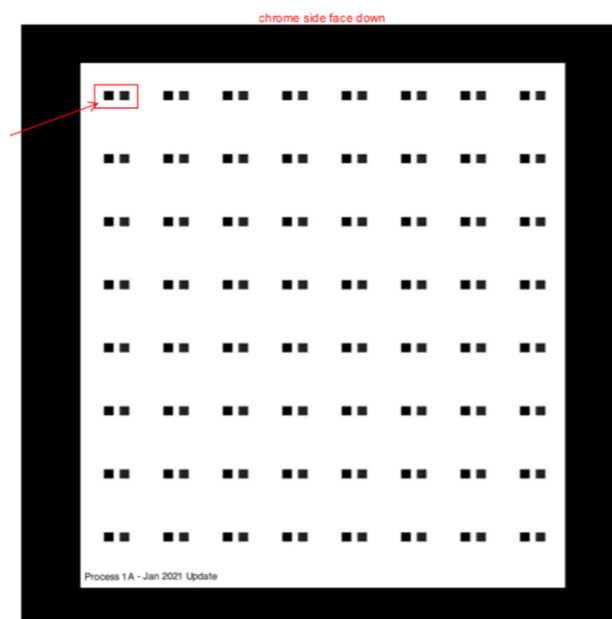
Figure A1. Schematic of a contact mask designed and utilized for the photolithography process to protect non-pixel active regions of the CIS chips.

Figure A2 shows a zoomed-in image of each square that consists of arrays of pixels. Pixel coverages on the left array have dimensions of $40 \times 40 \ \mu m^2$, and those on the right array have dimensions of $35 \times 35 \ \mu m^2$, as shown in Figure A3. Two different dimensions of pixel coverage have been designed to compensate for possible misalignment of the mask with the pixel active region due to the small nature of the said region.

Figure A2. Zoomed-in image of each square from Figure A1 that consists of arrays of pixels in the pixel active region. Each array has different dimensions of pixel coverage.
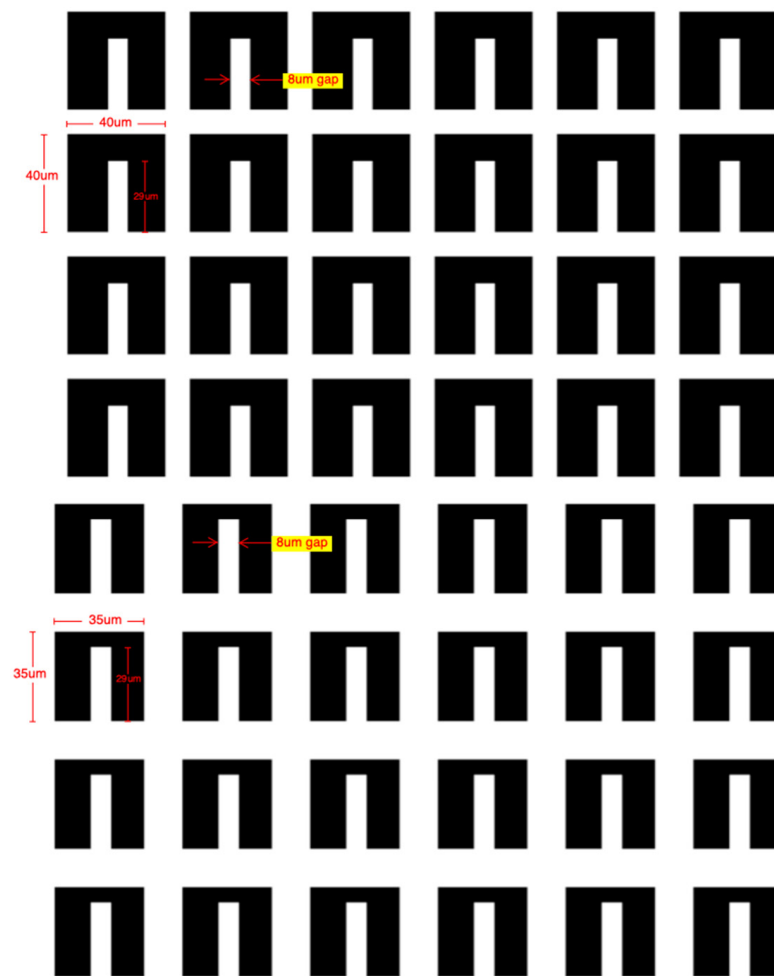

Figure A3. Zoomed-in image of the left array with $40 \times 40 \ \mu m^2$ pixel coverage (**top**) and the right array with $35 \times 35 \ \mu m^2$ pixel coverage (**bottom**) from Figure A2.

Appendix B

Due to material unavailability and sputter deposition chamber contamination concerns, even though the computational efforts presented in [1] used PbTe as the PAL material, a substitute inevitably had to be made for experimental efforts. A similar material in terms of Z number would ideally have to be selected as a substitute. Therefore, Bi_2Te_3 was eventually selected as the PAL material. To confirm that this material could function as intended during experimental efforts, the QY enhancement performance of 250 nm, 500 nm, and 1 μm Bi_2Te_3 PAL with 5 μm Si has been computationally compared, as can be seen in Figure A4. Although the QY enhancement from Si is not as great as that of PbTe, it provides affirmation that it will function as a substitute to experimentally demonstrate the PAL concept. Furthermore, 5 μm Si has been chosen for this comparison as the typical Si epi layer thickness of CIS chips is 5 μm [21,22].
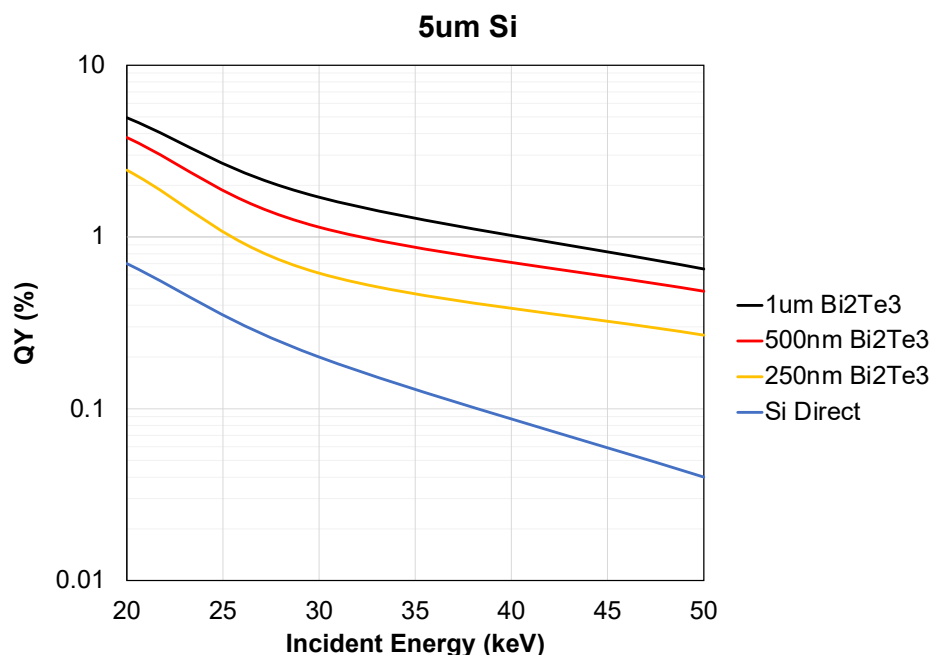

Figure A4. MCNP computational simulation results of QY vs. incident X-ray photon energy for 250 nm, 500 nm, and 1 μm Bi_2Te_3 PAL with 5 μm Si and Si direct detection with no Bi_2Te_3 PAL.

Appendix C

Prior to any high-energy X-ray radiation measurements, the noise of the pixels must be quantified. There are three main types of noise that must be quantified: fixed pattern noise (FPN), readout temporal noise (readout noise; RTN), and pixel noise (PN).

FPN captures the spatial variance of the pixel readout circuits. It is essentially considered sensor imperfections and consistent non-uniformities between pixels (e.g., offsets/threshold mismatches from the transistors). It is quantified by the standard deviation of spatial variation in pixel outputs after averaging 300 frames taken with imaging mode off. By comparison, RTN describes the temporal variance of the pixels between repeated readouts. It is determined by the standard deviation of the difference between the images taken at each frame with imaging mode off and the FPN raw image, the latter being the image averaged over all the 300 frames to quantify FPN, as mentioned earlier. PN, the noise at the chip output, is calculated by rearranging Equation (1). Taking the standard deviation of the PN is essentially determining the overall sensor noise, and taking the square of this standard deviation is considered noise variance. It should also be noted that Equation (1) often has shot noise on the right-hand side of the equation, but it is minimal and negligible as the images are taken in the dark to determine these values.
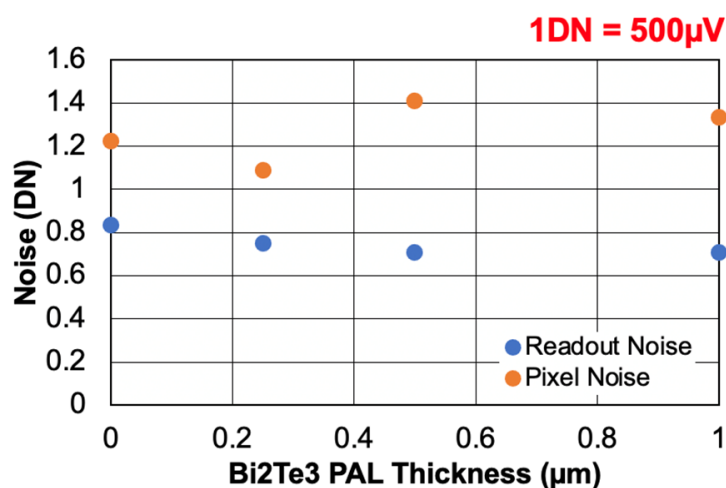
Figure A5. Plot of RTN (readout noise) and PN of chips #4, 9, 10, and 11. PAL-CIS chips with 500 nm and 1 μm Bi_2Te_3 PAL thicknesses have partial PAL coverage on the pixel active region due to partially successful liftoff. The PNs of these partial PAL coverage chips have slightly higher PNs, and it is uncertain whether the PNs will be reduced if the corresponding pixel active regions are completely covered. However, the noise values for all four chips appear to be either similar or within the same order of magnitude.

References

1. Lee, E.; Anagnost, K.M.; Wang, Z.; James, M.R.; Fossum, E.R.; Liu, J. Monte Carlo Modeling and design of photon energy attenuation layers for >10x quantum yield enhancement in Si-based hard X-ray detectors. *Instruments* **2021**, *5*, 17. [CrossRef]
2. Lee, E. Towards the Photonic Efficiency Enhancement of Solar-Selective Absorbers and Si-Based High-Energy X-ray Detectors. Ph.D. Thesis, Dartmouth College, Hanover, NH, USA, 2021.
3. Wang, Z. On the single-photon-counting (SPC) modes of imaging using an XFEL source. *J. Instrum.* **2015**, *10*, C12013. [CrossRef]
4. Wang, Z.; Anagnost, K.; Barnes, C.W.; Dattelbaum, D.M.; Fossum, E.R.; Lee, E.; Liu, J.; Ma, J.J.; Meijer, W.Z.; Nie, W.; et al. Billion-pixel X-ray camera (BiPC-X). *Rev. Sci. Instrum.* **2021**, *92*, 043708. [CrossRef] [PubMed]
5. Shimura, F. Silicon crystal growth and wafer preparation. In *Semiconductor Silicon Crystal Technology*; Elsevier: Amsterdam, The Netherlands, 2012; p. 198.
6. Robinson, S.P. X-ray Physics, Massachusetts Institute of Technology. 2007. Available online: http://web.mit.edu/8.13/www/JLExperiments/JLExp31.pdf (accessed on 1 August 2021).
7. Fenelon, A.G.R. A X-ray Scanning Machine for Imaging Atomic Elements. Master's Thesis, National Institute of Higher Education, Dublin, Ireland, 1988; p. 39. Available online: https://core.ac.uk/download/pdf/147605209.pdf (accessed on 1 August 2021).
8. Li, Z. Radiation damage effects in Si materials and detectors and rad-hard Si detectors for SLHC. *J. Instrum.* **2009**, *4*, P03011. [CrossRef]
9. Wheeler, D.C.; Bingham, E.; Winer, M.; Conrad, J.M.; Robinson, S.P. Observation of relativistic corrections to Moseley's law at high atomic number. *arXiv* **2018**, arXiv:1809.10480.
10. Lecture 8—Characterization. Available online: https://www.uio.no/studier/emner/matnat/ifi/IN5350/h20/timeplan/in5350_h20_8_characterization2.pdf (accessed on 6 October 2021).
11. Avalanche Statistics. Available online: https://indico.cern.ch/event/35172/contributions/1754354/attachments/695985/955670/AvalancheStatisticsRD51Paris.pdf (accessed on 7 September 2021).
12. He, Z.; Yang, J. Identification and reconstruction of single-pixel incomplete charge collection events. *IEEE Trans. Nucl. Sci.* **2013**, *60*, 2.
13. Buttacavoli, A.; Principato, F.; Gerardi, G.; Cascio, D.; Raso, G.; Bettelli, M.; Zappettini, A.; Seller, P.; Veale, M.C.; Abbene, L. Incomplete charge collection at inter-pixel gap in low-and high-flux cadmium zinc telluride pixel detectors. *Sensors* **2022**, *22*, 1441. [CrossRef] [PubMed]
14. Zhao, S.; Lioliou, G.; Butera, S.; Krysa, A.B.; Barnett, A.M. AlInP X-ray photodiodes without incomplete charge collection noise. *Nucl. Instrum. Methods Phys. Res. Sect. A Accel. Spectrometers Detect. Assoc. Equip.* **2020**, *960*, 163606. [CrossRef]
15. Butera, S.; Lioliou, G.; Krysa, A.B.; Barnett, A.M. InGaP (GaInP) mesa p-i-n photodiodes for X-ray photon counting spectroscopy. *Sci. Rep.* **2017**, *7*, 10206. [CrossRef] [PubMed]

16. Beck, P.; Cherepy, N.; Payne, S.A.; Hunter, S.L. Advancements in gamma spectrometers based on europium-doped strontium iodide and characterization of its gamma and electron response. In Proceedings of the 2014 IEEE Nuclear Science Symposium and Medical Imaging Conference (NSS/MIC), Seattle, WA, USA, 8–15 November 2014.

17. Desjardins, K.; Popescu, H.; Mercere, P.; Menneglier, C.; Gaudemer, R.; Thanell, K.; Jaouen, N. Characterization of a back-illuminated CMOS camera for soft x-ray coherent scattering. *AIP Conf. Proc.* **2019**, *2054*, 060066.

18. Wang, Z. Advanced X-ray Methods for PMI in MFE. Available online: https://permalink.lanl.gov/object/tr?what=info:lanl-repo/lareport/LA-UR-21-32331 (accessed on 12 August 2023).

19. VITA 5000 5.3-Megapixel 75 FPS Global Shutter CMOS Image Sensor. Available online: https://www.onsemi.com/pdf/datasheet/noiv1sn5000a-d.pdf (accessed on 4 September 2021).

20. Owens, A. *Semiconductor Radiation Detectors*; CRC Press, Taylor et Francis Group: Boca Raton, FL, USA; London, UK; New York, NY, USA, 2021.

21. Performance of Epitaxial Layer in CMOS Devices. Available online: https://meroli.web.cern.ch/lecture_CMOS_APS_epilayer.html/ (accessed on 4 September 2021).

22. CMOS Image Sensor Device and Fabrication. Available online: http://isl.stanford.edu/~abbas/ee392b/lect05.pdf (accessed on 4 September 2021).

23. Xie, S.; Sun, Q.; Ying, G.; Guo, L.; Huang, Q.; Peng, Q.; Xu, J. Ultra-precise surface processing of LYSO scintillator crystals for positron emission tomography. *Appl. Surf. Sci.* **2019**, *469*, 573–581. [CrossRef] [PubMed]

24. Lu, L.; Sun, M.; Wu, T.; Lu, Q.; Chen, B.; Huang, B. All-inorganic perovskite nanocrystals: Next-generation scintillation materials for high-resolution x-ray imaging. *Nanoscale Adv.* **2022**, *4*, 680–696. [CrossRef] [PubMed]

25. Chen, X.; Liu, B.; Zhu, J.; Gu, M.; Chen, H.; Liu, J.; Chen, L.; Ouyang, X. Light extraction enhancement and directional control of scintillator by using micronlens arrays. *Opt. Express* **2018**, *26*, 18.

26. Park, C.H.; Kang, S.W.; Jung, S.; Lee, D.J.; Park, Y.W.; Ju, B. Enhanced light extraction efficiency and viewing angle characteristic of microcavity OLEDs by using a diffusion layer. *Sci. Rep.* **2021**, *11*, 3430. [CrossRef]

27. Zhang, X.; Xie, J.; Zhang, Y.; Sun, R.; Liu, S.; Zhang, W.; Zhang, X.; Hu, F. PMMA-doped composite films microlens arrays on a flexible substrate for improving extraction of an organic light-emitting diode. *Appl. Opt.* **2022**, *61*, 4. [CrossRef] [PubMed]

28. The Advanced Photon Source Research Techniques. Available online: https://www.aps.anl.gov/Beamlines/Research-Techniques (accessed on 7 September 2021).

29. The Advanced Photon Source Beamline 1-BM-B,C: Optics & Detector Testing. Available online: https://www.aps.anl.gov/Beamlines/Directory/Details?beamline_id=1 (accessed on 7 September 2021).

30. High-Caliber Research Launches NSLS-II Beamline into Operations. Available online: https://www.bnl.gov/newsroom/news.php?a=212833 (accessed on 12 August 2023).